JOURNAL OF GEOPHYSICAL RESEARCH, VOL. 112, D24S14, doi:10.1029/2007JD008449, 2007

Impact of ice supersaturated regions and thin cirrus on radiation in the midlatitudes

F. Fusina,[1] P. Spichtinger,[1] and U. Lohmann[1]

Received 18 January 2007; revised 20 July 2007; accepted 31 August 2007; published 15 December 2007.

[1] In this study we investigate the radiative impact of ice supersaturated regions (ISSRs, i.e., cloud free air masses in the upper troposphere that are supersaturated with respect to ice) and thin cirrus. For this purpose we use corrected radiosonde data obtained from routine measurements over the meteorological observatory in Lindenberg, Germany. The radiative effect of the measured ice supersaturation is determined. By constructing an idealized profile from the measurement data the radiative properties of ISSRs and thin cirrus containing ice supersaturation were studied. The impact of ISSRs on the surface forcing is negligible but locally, within the vertical profile, changes in the heating rates up to 1 K d^{-1} for typical values of 130% relative humidity with respect to ice compared to the saturated profiles are found. This is also important for the local dynamics within the supersaturated layers. The outgoing longwave radiation due to the enhanced water vapor content inside ISSRs decreases up to 0.8 W m^{-2}. The radiative impact of thin cirrus is much stronger. Thin cirrus influence the surface budget, the top of the atmosphere radiation and the vertical profile of the heating rates. Changes in the outgoing longwave radiation and in the reflected shortwave flux at top of the atmosphere up to 64 W m^{-2} and 79 W m^{-2}, respectively, are possible. Changes in the surface flux (downward) up to 89 W m^{-2} are found. The maximal heating rate differences between thin cirrus and ISSR amount to 15 K d^{-1}. The radiative impact of thin cirrus clouds depends strongly on cloud ice content and the size of the ice crystals. Additionally, the radiative impact of cirrus formed by parameterizations not allowing ice supersaturations in large-scale models is estimated. The errors due to artificially formed cirrus are quite large; differences up to 3 K d^{-1} in the vertical heating profiles and up to 38 and 40 W m^{-2} in the outgoing longwave radiation and the surface flux, respectively, are found. Thus we recommend using physically based parameterizations in GCMs which allow ice supersaturation.

Citation: Fusina, F., P. Spichtinger, and U. Lohmann (2007), Impact of ice supersaturated regions and thin cirrus on radiation in the midlatitudes, *J. Geophys. Res.*, *112*, D24S14, doi:10.1029/2007JD008449.

1. Introduction

[2] The existence of cloud-free air masses that are supersaturated with respect to (wrt) ice in the upper troposphere or lowermost stratosphere is known since almost 60 a. *Glückauf* [1945] found from hygrometer data obtained over Southern England that very high ice supersaturations (i.e., values up to 160% relative humidity wrt ice) occur frequently in the upper troposphere. However, probably the first observations of ice supersaturation were made by Alfred Wegener. During his second expedition to Greenland in 1911/1912 [*Wall*, 1942] he recognized that moist breathing of his horses produced small ice crystals. These insights from the first part of the 20th century were neglected for many years, and measurements reporting ice supersaturation often were termed as errors. During the last decade the existence of air masses in the status of supersaturation was proven by many measurements with a variety of different measurement techniques [e.g., *Jensen et al.*, 1998; *Vay et al.*, 2000; *Ovarlez et al.*, 2000]. Theoretical considerations are consistent with the existence of ice supersaturation because ice crystals form at very high supersaturations, the exact freezing thresholds depend on the formation mechanism (homogeneous freezing of solution droplets or heterogeneous nucleation) [e.g., *Koop et al.*, 2000; *DeMott et al.*, 2003]. For homogeneous nucleation, which is probably the dominant mechanism for forming ice crystals at low temperatures ($T < -38°C$) relative humidities in the range 140–170% RHi, depending on temperature [*Koop et al.*, 2000], are required. For heterogeneous nucleation, the freezing thresholds are smaller, probably in the range 110–140%RHi [e.g., *Möhler et al.*, 2006; *DeMott et al.*, 2003].

[3] The properties and global distributions of ice supersaturated regions (ISSRs) were discovered during the last years [e.g., *Gierens et al.*, 1999, 2000; *Spichtinger et al.*, 2003a, 2003b; *Gettelman et al.*, 2006]. However, the

[1]Institute for Atmospheric and Climate Science, ETH Zurich, Zurich, Switzerland.

0148-0227/07/2007JD008449$09.00

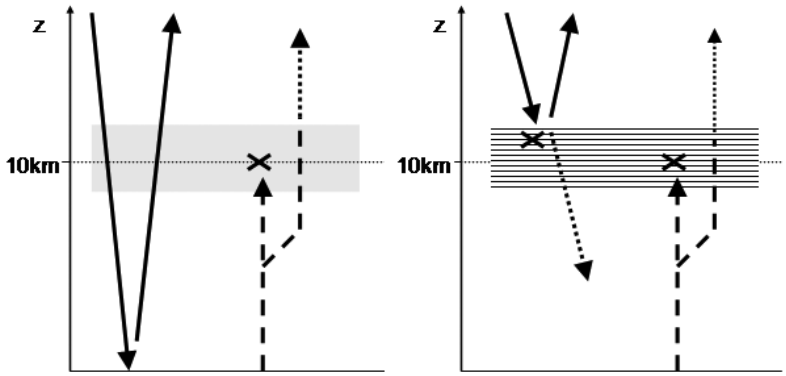

Figure 1. Radiative impact of ISSRs and thin cirrus. (left) ISSRs. The incoming solar radiation (solid) is not affected by ISSRs, whereas the outgoing infrared radiation (dashed) is partly absorbed by the enhanced water vapor concentration; the transmitted radiation is indicated by a dotted line. (right) Thin cirrus. Here both the solar (solid) and infrared (dashed) radiation are affected by the ice crystals; transmission is again indicated by a dotted line.

radiative impact of ISSRs has not been investigated so far. This is surprising because in ISSRs the water vapor content is much higher than in the subsaturated environment. Water vapor is a very effective greenhouse gas and it constitutes a positive feedback to the forcing from well-mixed greenhouse gases [see, e.g., *Forster and Gregory*, 2006; *Soden et al.*, 2005]. ISSRs frequently occur in the upper troposphere. For example, routine aircraft measurements suggest, that ISSRs occur 20–30% of the time in cloud free air masses over the North Atlantic [*Gierens et al.*, 2000]. Because of the large horizontal extensions of ISSRs (on average 150 ± 250 km [*Gierens and Spichtinger*, 2000]) there is a substantial amount of cloud free air masses with enhanced water vapor content.

[4] ISSRs are potential formation regions of cirrus and persistent contrails. These clouds are important modulators of the radiation budget [*Quante*, 2004]. The contribution of thin cirrus to Earth' radiation budget is not well known, but it is assumed that they contribute to a net heating of the Earth-atmosphere system [e.g., *Chen et al.*, 2000].

[5] There is a principle difference in the radiative impact of ISSRs and cirrus (see Figure 1): In case of a cloud free ice supersaturated layer the incoming solar radiation passes through the supersaturation layer with hardly any absorption. On the other hand the outgoing longwave radiation is partly absorbed by the enhanced water vapor inside the ISSR. Hence ISSRs have only a significant effect on the longwave radiation. In the case of thin cirrus the incoming solar radiation is (partly) scattered by the ice crystals, part of the outgoing longwave radiation is absorbed by the ice crystals. If there is supersaturation inside the cirrus cloud layer (which is frequently found in many data sets, see below) the effect of absorbing longwave radiation due to enhanced water vapor also contributes to the radiative effect on thin cirrus.

[6] Although the existence of ice supersaturated regions was proven by theoretical considerations and measurements and ice crystal nucleation takes place at (high) ice supersaturations, in general circulation models (GCMs) usually ice clouds are formed at ice saturation. There are only few climate models which allows ice supersaturation [*Lohmann and Kärcher*, 2002; *Gettelman and Kinnison*, 2006; *Liu et al.*, 2007] and one version of the ECMWF numerical weather model [*Tompkins et al.*, 2007].

[7] In this study we investigate the radiative impact of ISSRs and thin cirrus as well for the radiation budget as for the vertical heating rates. For this purpose we use radiosonde data which were previously used for investigations of the properties of ISSRs by *Spichtinger et al.* [2003a], obtained over the meteorological observatory in Lindenberg, Germany. Hence our estimations are representative only for the midlatitudes. We also discuss the possible errors due to artificially formed cirrus in GCMs using idealized vertical profiles.

[8] The structure of the paper is as follows: First, we describe our data, the data processing and the radiation model. In section 3 we present and discuss the results on the radiation impact of ISSRs and thin cirrus as well as the impact of cirrus formed at saturation in GCMs. In section 4 we give a short summary and some conclusions. In Appendix A, some formulas for calculating effective radii are derived.

2. Data Description, Processing, and Model Description

2.1. Data Description

[9] We use radiosonde data obtained from routine ascents of Vaisala RS 80A radiosonde at the meteorological observatory in Lindenberg, Germany. The usage of the standard radiosonde RS 80A with "humicap" humidity sensors (capacitive sensors) is usually afflicted with errors in the low temperature range $T \leq -30°C$, which results in a tremendous underestimation of the relative humidity with respect to ice. The radiosonde data were corrected using a method developed by *Leiterer et al.* [2005]. Hence, with this correction, it is possible to detect ice supersaturation from the radiosonde data [*Spichtinger et al.*, 2003a], although the amount of supersaturation is markedly underestimated: The maximum values are always lower than 140% RHi. Unfor-

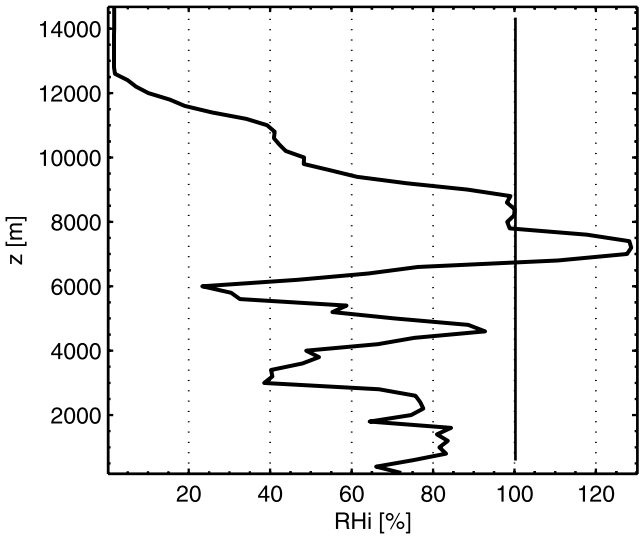

Figure 2. Relative humidity profile over ice (RHi) versus altitude (z) obtained from routine ascent of Vaisala RS 80A on 12 March 2001 at 1200 UTC over Lindenberg, Germany.

tunately, there is no direct comparison of corrected RS 80A profiles with other in situ measurements like, e.g., frost point hygrometers. We know, however, from in situ observations with other measurement techniques, that in the midlatitudes values of relative humidity up to 160–170% RHi are possible and quite frequently [e.g., *Jensen et al.*, 1998; *Ovarlez et al.*, 2002; *Spichtinger et al.*, 2004; *Comstock et al.*, 2004]. This is also consistent with theoretical considerations for homogeneous freezing [e.g., *Koop et al.*, 2000].

[10] We use data from the time period February 2000 until April 2001 for the standardized dates 0000, 0600, 1200 and 1800 UTC. This results in 1563 vertical profiles including the variables temperature (T), pressure (p), altitude (z) and relative humidity with respect to water (RH). Every measurement value corresponds to the mean value of 10 measurements within 10 s; together with the mean vertical upward velocity of the sonde of about 5 m s^{-1} this results into a vertical resolution of about 50 m. The relative humidity with respect to ice (RHi) was calculated for temperatures $T < 0°C$ from the variables T and RH as in the work by *Spichtinger et al.* [2003a]. Figure 2 shows a typical RHi profile. The uncertainty in the temperature measurement is $\Delta T = \pm 0.1$ K [*Antikainen and Jauhiainen*, 1995]. For the relative humidity, the relative uncertainty compared to a research radiosonde is estimated to be $\Delta RH = \pm 1.9\%$ [*Spichtinger et al.*, 2003a].

2.2. Data Processing and ISSR Statistics

[11] The high-resolution data were first interpolated polynomially on a fixed vertical grid with spacing of 200 m. This is necessary because the GCM radiation model we use later is designed for coarse vertical resolutions. Additionally, we only use vertical profiles with a complete recording from the surface to approximately 15 km. The detection of ISSRs has been carried out as by *Spichtinger et al.* [2003a]: A radiosonde crossing an ensemble of supercooled water droplets would report $RH = 100\%$ which implies ice supersaturation but this is neither an ISSR nor a cirrus cloud. Hence we use a ''dynamical'' criterion to register an ISSR. Its bottom temperature needs to be lower than −30°C and simultaneously its top temperature needs to be lower than −35°C. This criterion avoids counting profiles containing supercooled water. It is derived from the findings that clouds at temperatures below −30°C contain almost no supercooled water droplets [e.g., *Pruppacher*, 1995; *Verlinde et al.*, 2007]. The choice of the top temperature of $T = -35°C$ coincides with the temperature regime of homogeneous freezing [*Pruppacher*, 1995]. However, the criterion is not a cloud clearing, i.e., the profiles could be contaminated with cirrus. For our first investigation we now assume that all these layers are cloud free. Using this criterion we find 401 ISSRs in 1563 vertical profiles. From these we only use single layer ISSRs for further investigation, 293 out of the original number of ISSRs are single layer ISSRs.

[12] From the data some information on the shape of the layers could be obtained: Figures 3a–3c show frequency distributions of vertical extension (d), mean altitude of the center of the ISSR (z_c) and maximum RHi (RHi_{max}), respectively, measured by the radiosondes. Mean values are as follows: $\overline{d} \pm \sigma_d$ 850 ± 740 m, $\overline{r_c} \pm \sigma_r = 8200 \pm 1450$ m and $\overline{RHI}_{max} \pm \sigma_{RHi} = 108 \pm 6.5\%$. For more details, refer to *Spichtinger et al.* [2003a].

2.3. Idealized Profiles

[13] In order to obtain average information of the radiative properties of ISSRs we define an idealized profile: From all radiosonde profiles containing a single layer ISSR we compute mean temperature and pressure profiles. The tropopause of the average idealized profile is at $z_{TP} \sim 12000$ m. The mean profile for the relative humidity has been constructed in a more sophisticated way: The altitude and thickness for the ISSR were determined by the average values presented in section 2.2 and in Figures 3a–3d. The center of the ISSR is located at the averaged altitude of $z_c \approx 8200$ m. For the radiative impact of ISSRs we estimate an upper value to be compared with the radiative impact of cirrus in section 3.2. Therefore we choose a vertical extension $d = 1200$ m, which is slightly larger than the mean value. On the other hand later we ''form'' a cirrus by filling the supersaturated layer with ice crystals. For this cirrus, a vertical extension of 1.2 km is on the low end of typical observed values [*Dowling and Radke*, 1990; *Mace et al.*, 2006]. This enables us to compare the impact of supersaturated layers with and without ice crystals. For the maximum value of RHi we choose a value of $RHi = 130\%$. Because radiosondes typically underestimate RHi, this value stems from in situ measurements [*Ovarlez et al.*, 2002]. Additionally, we varied the shape (rectangular versus peak) and the maximal value of RHi (100–130%RHi) (Figure 4) for sensitivity studies. Below the supersaturated layer we assume a constant value of $RHi = 60\%$, above the layer up to the tropopause also a constant value is assumed ($RHi = 40\%$), then further up the specific humidity reaches typical stratospheric values (∼1–10 ppm).

[14] For investigation of thin cirrus (i.e., clouds consisting completely of ice crystals with optical depths <1.) including ice supersaturation we artificially introduce cloud ice and different number densities of ice crystals into the ice supersaturated layer as described below. By varying the ice crystal number density and the total ice water content,

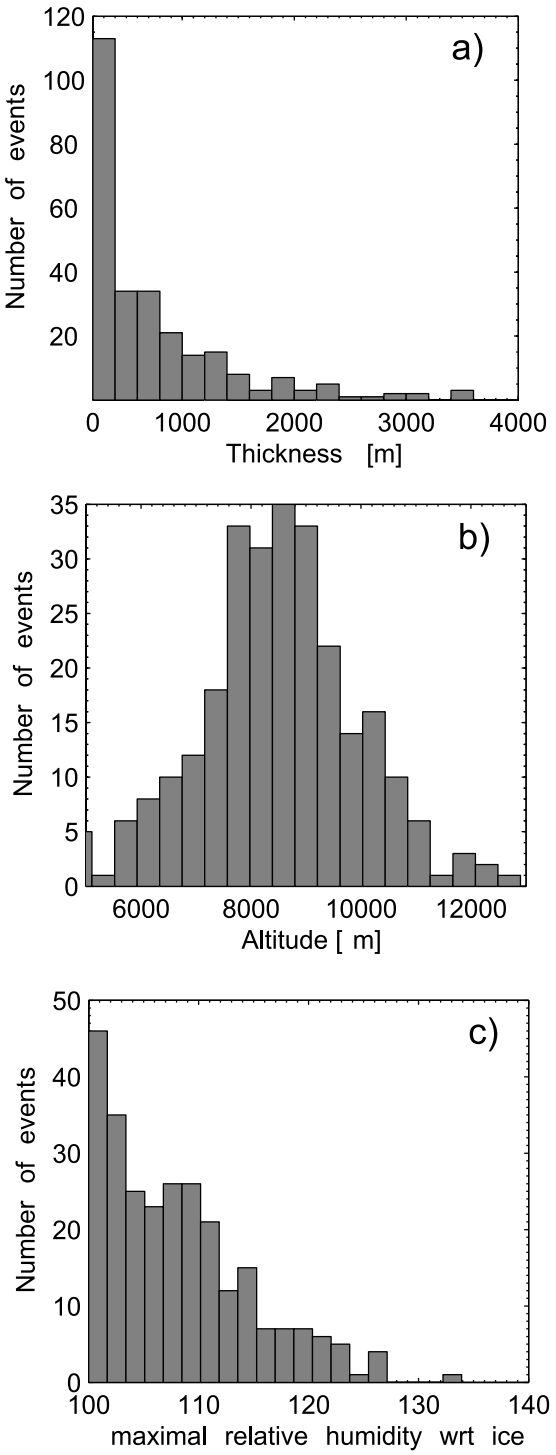

Figure 3. Distributions of the (a) vertical extension, (b) mean altitude and (c) maximum RHi of ISSRs obtained from 293 radiosonde profiles containing single layer ISSRs.

we achieve a possible range of the possible radiative impact of thin cirrus.

2.4. Radiation Model

[15] The radiation code used in this study is the radiative transfer code of the Canadian Centre for Climate Modelling and Analysis (CCCma) as used in a single column model (SCM) study [*Lohmann et al.*, 1999]. For our one step calculations we only use the radiative transfer calculations of the model without any dynamics or microphysics. The radiation code is based on a two-stream approximation using four bands in the solar regime and six bands in the thermal infrared. The required optical ice parameters are the volume extinction coefficient, the single-scattering albedo, and the asymmetry factor. They are parameterized as a function of the ice crystal effective radius and the ice water content following *Slingo* [1989], *Dobbie et al.* [1999] and *Fu* [1996]. For the prescribed values of ice water content we use a "reference value" from a fit to several measurements by *Schumann* [2002, equation (1)]:

$$\mathrm{IWC}_{ref} = \exp(6.97 + 0.103 \cdot T(^{\circ}C)), \tag{1}$$

which can be regarded as a mean IWC inside cirrus in midlatitudes. We assume that the ice crystal size is lognormally distributed:

$$f(L) = \frac{N}{\sqrt{2\pi} \cdot \log \sigma_L} \cdot \exp\left(-\frac{1}{2} \left(\frac{\log\left(\frac{L}{L_m}\right)}{\log \sigma_L} \right)^2 \right) \tag{2}$$

where N denotes the ice crystal number density and L_m is the modal size; σ_L denotes the geometrical standard deviation. For the width of the distribution we assume a geometrical standard deviation of $\sigma_L = 1.5$ (M. DeReus, personal communication, 2007). The moments of the distribution can be expressed as $\mu_k[L] = N \cdot L_m^k \exp(0.5(k\log\sigma_L)^2)$; hence the value of L_m can be derived from the mean size of the ice crystals using the definition by moments: $L_{mean} = \frac{\mu_1[L]}{\mu_0[L]} = L_m \exp(0.5(\log\sigma_L)^2) \iff L_m = L_{mean}/\exp(0.5(\log\sigma_L)^2)$.

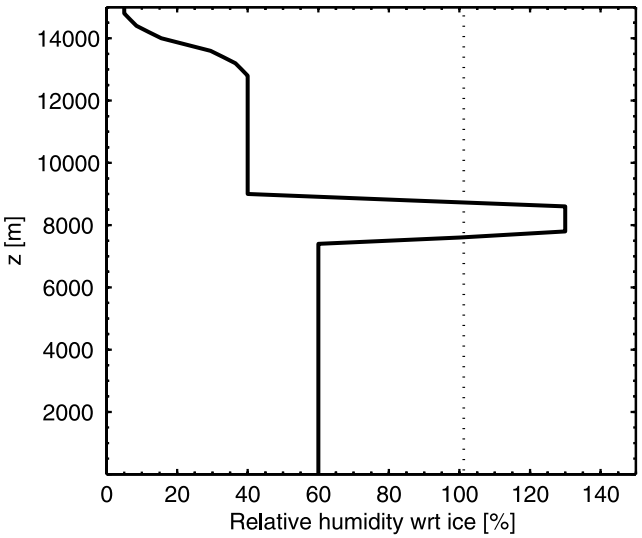

Figure 4. Idealized RHi profile obtained from 293 radiosonde profiles combining the mean altitude (see Figure 3b) and a typical vertical extension of ISSRs; mean altitude = 8200 m, maximum RHi = 130%. z denotes altitude.

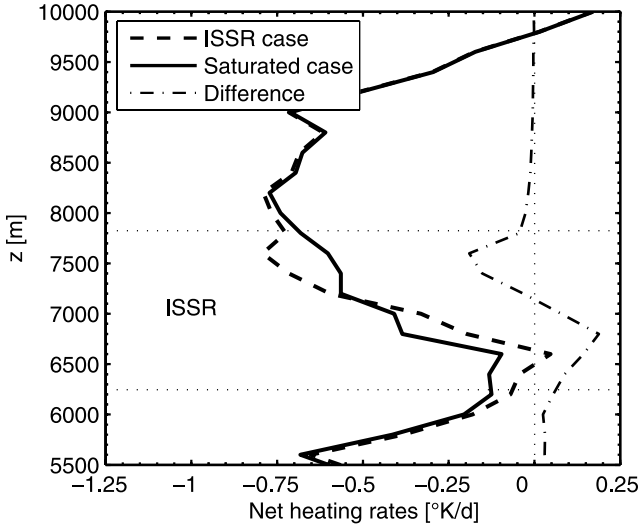

Figure 5. Net heating rates obtained from the radiosonde ascent on 12 March 2001 at 1200 UTC over Lindenberg, Germany, calculated with the radiation transfer model from the SCM CCCma. z denotes altitude.

[16] By using the mass-size relation by *Heymsfield and Iaquinta* [2000] for small columns

$$\left(\frac{m}{m_0}\right) = \alpha \cdot \left(\frac{L}{L_0}\right)^{\beta}; \alpha = 1.649 \cdot 10^3, \beta = 2.2, \qquad (3)$$

also the ice crystal mass is lognormally distributed. Here, m_0 = 1 g and L_0 = 1 cm denote unit mass and length, respectively. We use the mass-size relation to switch between the mean mass of ice crystals (given by IWC and N) and the size of the crystals, which is used for the calculation of the effective radius.

[17] The calculation of the ice crystal effective radius is based on the following equation [*Ebert and Curry*, 1992]:

$$r_{eff} = \frac{\int_0^\infty \left(\frac{A}{4\pi}\right)^{3/2} \cdot f(L)\, dL}{\int_0^\infty \frac{A}{4\pi} \cdot f(L)\, dL} \qquad (4)$$

where A denotes the total surface of a hexagonal cylinder. We developed a way, to approximate this integral using only the (analytical) formula for the moments of the ice crystal size distribution as described in Appendix A. This formulation has the advantage that it is very easy to use different types of size distributions (e.g., gamma distribution) for sensitivity tests.

[18] The SCM uses the observed temperature, specific humidity and the derived ice water content and effective radius as input and assumes that the cloud fully occupies a layer; that is, the fractional cloud cover in our simulations is 1. For atmospheric trace gases and for the surface albedo (=17%), reference values from the ARM site in Oklahoma are used for consistency [*Zhang et al.*, 2005]. We repeated the calculations using the albedo for Lindenberg (=18.7%), causing only marginal differences. We use an average solar zenith angle of 60° at a geographical latitude of 52°N for Lindenberg (Germany).

3. Results and Discussion

3.1. Radiative Impact of Ice Supersaturated Regions

[19] For the investigation of the cloud free ISSRs we assume that all ice supersaturated layers found in the radiosonde data are cloud free. However, we have no evidence from this, because of lack of detection techniques for ice crystals on board of the radiosonde [see also *Spichtinger et al.*, 2003a]. In the next section we artificially introduce ice crystals into the ice supersaturated layer to simulate the impact of thin cirrus.

[20] A typical RHi profile of a radiosonde ascent over Lindenberg is shown in Figure 2. There we obtain a maximal value of the RHi of about 130% at an altitude between 7500 m and 8000 m. Using the CCCma SCM we obtain heating rates (longwave and shortwave) for the vertical profile and for top of the atmosphere (TOA) fluxes of the outgoing longwave radiation (OLR) and net shortwave radiation. Additionally, the radiation transfer was calculated for the saturated profile; that is, in the supersaturated layer the values were set to RHi = 100%. We define the ISSR Radiative Effect (IRE) as the difference between the maximum and the minimum value in the profile of the heating rate difference between the supersaturated and the saturated case, as indicated in equation (5):

$$\mathrm{IRE} := \max(Q(ISSR) - Q(sat)) - \min(Q(ISSR) - Q(sat)) \qquad (5)$$

where $Q(ISSR)$, $Q(sat)$ denote the heating rates of the supersaturated and the saturated profiles, respectively. This is a lower bound for the radiation impact of ISSRs because of the underestimation of ice supersaturation in spite of the correction.

[21] In principle, there is almost no effect on the incoming solar radiation due to the ISSR, only the outgoing longwave radiation is affected by absorption due to the (enhanced) water vapor within the layer. There is a strong warming in the lower part of the layer with enhanced water vapor due to the absorption of the longwave radiation from the surface. In the upper part of the supersaturation layer there is a cooling; this means that the water vapor molecules emit radiation into space.

[22] In Figure 5 the differences between the heating rates of the saturated and the supersaturated case of the example from Figure 2 are shown. At the lower boundary, the supersaturated case absorbs more longwave radiation and therefore its heating rate values are larger. At the upper boundary, we observe the opposite case, because the supersaturated layer emits more radiation than the saturated one, because of the higher amount of water vapor. By investigation of all 293 vertical profiles, it can be seen that the ISSR Radiative Effect IRE correlates very well with the maximal RHi (correlation coefficient: r = 0.91). Additionally, it can be seen that high values of RHi occur mainly in thicker ISSRs (Figure 6).

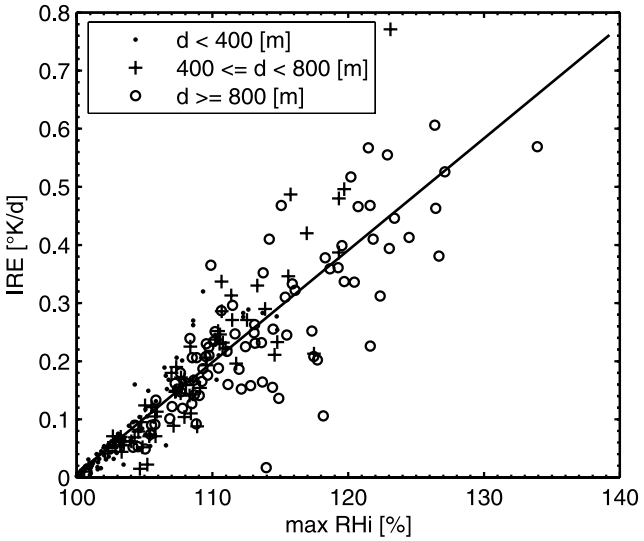

Figure 6. ISSR Radiative Effect (IRE) depending on the maximal relative humidity with respect to ice obtained from 293 radiosonde profiles containing single layer ISSRs.

[23] For a more detailed insight into the radiative properties of ISSRs we now vary the maximal RHi for three idealized profile (see Figure 4), a reference (saturated) case with RHi = 100% as the maximum value in the area of the "supersaturated layer," a supersaturated case (RHi = 130%) and a subsaturated case (RHi = 80%).

[24] The net heating rates of these three profiles are shown in Figure 7. For the reference case (i.e., saturated profile) the difference between the heating and the cooling peak is 0.83 K d^{-1}, in the supersaturated case the difference increases to 1.24 K d^{-1} (i.e., about 1.5 times larger than for the reference case), whereas in the subsaturated case the difference is reduced to 0.42 K d^{-1} (i.e., almost half of the value of the reference case). These values can be translated into the IRE; that is, for the supersaturated case IRE amounts to 0.56 K d^{-1} whereas for the subsaturated case the heating rates is reduced to $IRE = -0.41$ K d^{-1}.

[25] The ISSRs only have a negligible effect on the surface radiation budget, but we find a noticeable effect on the outgoing longwave radiation at the top of the atmosphere (TOA, see Figure 8): By varying the maximal RHi in the (super-) saturated layer from 60% to 160%, the OLR varies by about 0.8 W m^{-2} in the supersaturation range.

[26] For sensitivity studies we have changed the shape of the RHi profile from a rectangular shape to a triangular shape. The changes can mainly be seen in the LW cooling; in case of the peaked RHi profile the cooling is reduced marginally.

[27] Additionally, we have changed the RHi value above the ISSR in the range $20\% \leq RHi \leq 60\%$. Here we found, that for lower values of RHi (20%RHi) the cooling effect of the ISSR is enhanced (by a factor of 1.7), while for higher values (60%), the cooling is reduced (by a factor of 0.6). Observations suggest, that this strong decrease from supersaturation to low values above the ISSR (in our case to about 40%RHi) is very common [see also *Spichtinger et al.*, 2005a, 2005b].

3.2. Radiative Impact of Thin Cirrus

[28] Now we include cloud ice into the supersaturated layer in order to determine the impact of thin cirrus (with ice supersaturation inside). Thin cirrus are hard to detect, hence they can be a source of errors for remote sensing applications (e.g., for the detection of aerosol optical depths in a range of $\tau = 0.1-0.3$).

[29] Although we now include ice crystals into our vertical profile we do not set RHi = 100% inside the cloud. There is evidence from measurements, that (moderate) ice supersaturations are frequently found inside (thin) cirrus [see, e.g., *Ovarlez et al.*, 2002; *Spichtinger et al.*, 2004; *Peter et al.*, 2006].

[30] We vary the ice water content (IWC) and the ice crystal number density. These two parameters determine the microphysical structure of the cirrus cloud. The values for IWC range between 1% and 100% of the reference value given by equation (1). Implicitly, we also consider a change

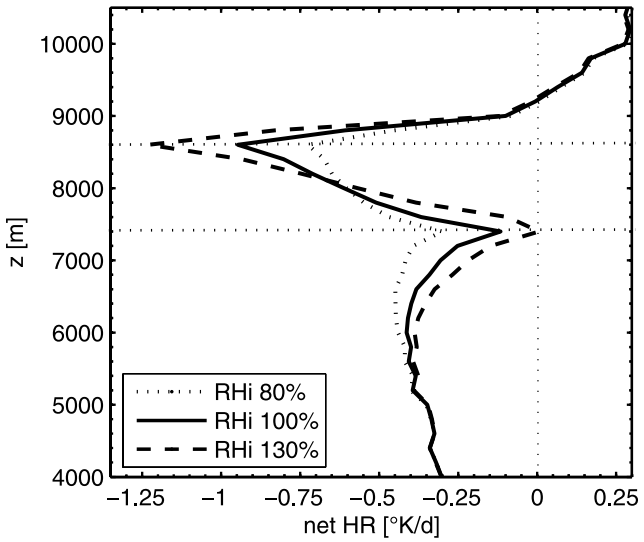

Figure 7. Net heating rates for idealized profiles: (1) Subsaturated layer with RHi = 80%, (2) saturated layer, reference case and (3) supersaturated layer with RHi = 130%.

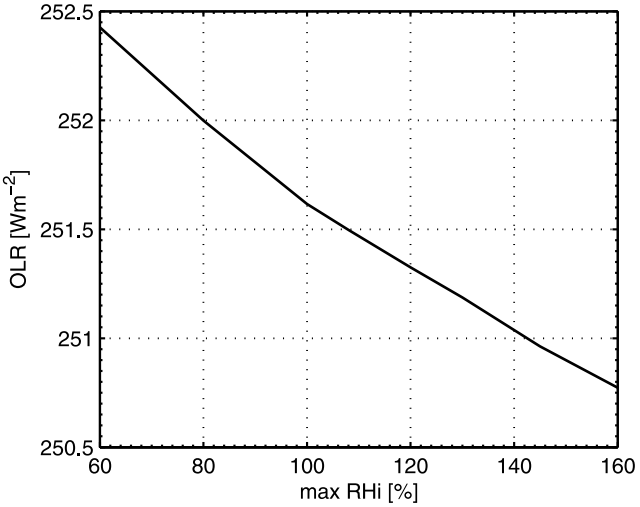

Figure 8. Changes in the outgoing longwave radiation at the top of the atmosphere depending on the maximal value of RHi in the idealized profiles.

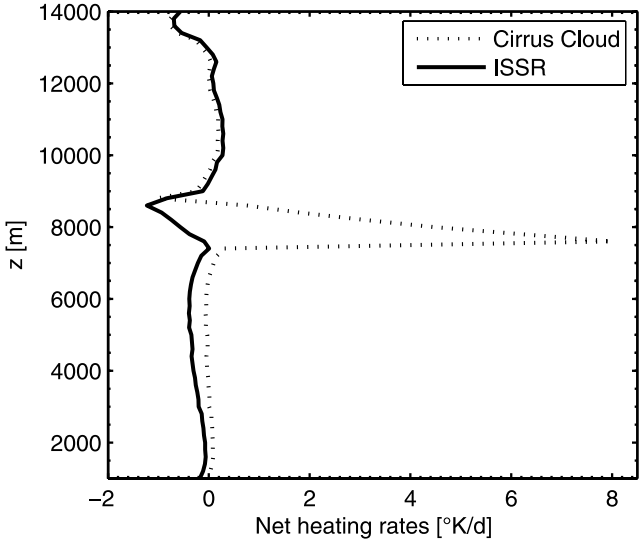

Figure 9. Net heating rates for an idealized ISSR and a thin cirrus cloud (50% IWC_{ref}, N = 1000 L^{-1}, optical depth τ = 0.84, *RHi* = 130%). z denotes altitude.

of IWC in altitude because of the temperature dependence of the reference value. The ice crystal number density N varies between 20 and 1000 crystals per liter being representative for midlatitudes [e.g., *Quante*, 2004]. From both variables the mean mass and mean size of the ice crystals is calculated. Then, the effective radius r_{eff} can be calculated using equation (4).

[31] Figure 9 shows the differences in the net heating rates between a cloud free ice supersaturated layer and the same layer including a cirrus cloud: Whereas for the cloud free ISSR only the longwave radiation is absorbed by the enhanced water vapor within the layer, in case of a cloudy layer the ice crystals additionally absorb energy in both frequency bands (longwave and shortwave) and the incoming solar radiation is partly reflected. Hence the heating effect within the cloudy layer is much higher than in the clear air case (with differences of +8 K d^{-1} in this case and values up to +15 K d^{-1} for the whole study). In the case of cirrus a nonnegligible effect on the surface radiation budget can be observed with changes up to 89 W m^{-2}.

[32] At the top of the atmosphere the radiative flux changes by a noticeable amount. Here, differences between the cloud free profile and the cloudy profile in the OLR

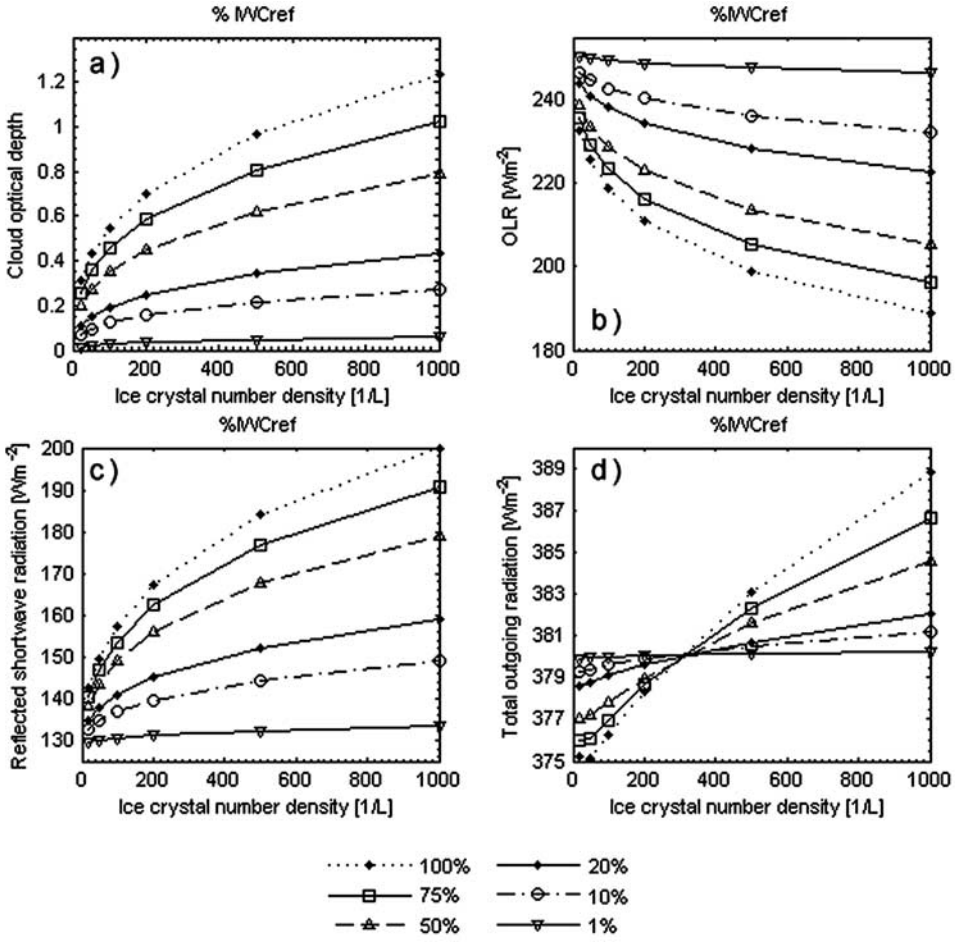

Figure 10. (a) Optical depth, (b) outgoing longwave radiation TOA, (c) reflected shortwave radiation at TOA and (d) total outgoing radiation at TOA of the simulated cirrus (thickness = 1200 m) for different values of IWC (the percentages denote % of IWC_{ref}, equation (1)) and ice crystal number density (in L^{-1}).

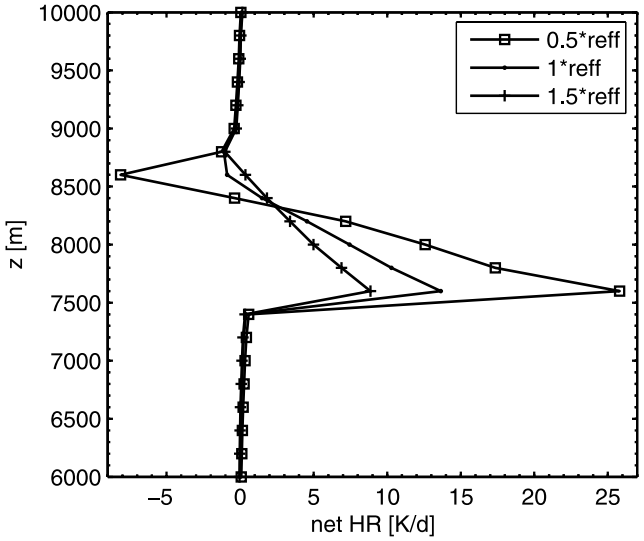

Figure 11. Heating rates for different "habits" of ice crystals, i.e., for different correction values f to the effective radius, i.e., $r'_{eff} = f \cdot r_{eff}$ for ice crystal number densities of N = 1000 L^{-1} and IWC = 100% IWC_{max}.

reach values up to 64 W m^{-2}. Because of increasing values of IWC and ice particles number density the cloud optical depth and albedo are increasing too. More radiation is absorbed at the bottom of the cloud (warming), and also more solar radiation is reflected at the top of the cloud (cooling). Here, the differences in the reflected shortwave radiation reaches values up to 79 W m^{-2}.

[33] Figures 10a–10d show the changes of the optical depth and the fluxes as a function of the IWC and the ice particle number density.

[34] The optical depth depends strongly on both, cloud ice and ice crystal number density. For a given ice water content, the optical depth weakly increases for increasing number concentration, i.e., for decreasing effective radius due to stronger scattering at more small crystals (Figure 10a). This is the main feature, which influences also the OLR (Figure 10b) and the reflected shortwave radiation (Figure 10c). Because of the more efficient absorption of longwave radiation emitted from the surface at the bottom of the cirrus layer and less at the cloud top, the OLR decreases with increasing ice crystal number density at constant IWC values. By using Figure 10a, this means that the OLR decreases with increasing optical depth. For the reflected shortwave radiation it is the other way round: The reflected shortwave radiation increases with increasing optical depth. The question arises which of these two effects is dominant for different values of IWC and ice crystal number density, i.e., in which regimes a net warming or cooling can be observed. For this purpose we investigate the total outgoing radiation (Figure 10d): The total outgoing radiation is defined as the sum of the OLR and the reflected shortwave radiation. For clouds with less than 320 ice crystals per liter the total outgoing radiation is lower than for thicker clouds (increased IWC, larger crystals). The reason for this warming effect is that the amount of absorbed longwave radiation is larger than the reflected shortwave radiation. For clouds with more than 320 ice crystals per liter the opposite effect is found. Now, the loss of energy by reflecting shortwave radiation dominates the longwave radiation absorption and leads to a general cooling effect. This value of $N = 320\ L^{-1}$ should only be regarded as a qualitative indicator, that at some point there is a transition from heating to cooling induced by the cirrus cloud [see also *Stephens and Webster*, 1981]. The transitions between warming and cooling depends on the ice crystal mass and number densities. However, it is also expected that this transition depends on the altitude, i.e., on the temperature of the cirrus.

[35] We tested the sensitivity of our results to the choice of the size distribution and the habit of the ice crystals. Instead of a lognormal distribution we used a gamma distribution of the following type:

$$f(L) = \frac{N}{\Gamma(r)} \left(\frac{L}{L_g}\right)^r \exp\left(-\frac{L}{L_g}\right) \frac{1}{L} \tag{6}$$

with parameters r and L_g; Γ denotes the gamma function. The moments of the distribution can be calculated by $\mu_k[L] = N \cdot L_g^k\, \Gamma(r+k)/\Gamma(r)$. In fact, L_g can be derived from the mean size of the ice crystals using the definition via moments as $L_{mean} = \frac{\mu_1[L]}{\mu_0[L]} = L_g \cdot r \iff L_g = L_{mean}/r$. A value of $r = 3$ could be used for a gamma size distribution of ice crystals [*Wyser*, 1998]. In our calculations, we found that there are almost no differences in the calculations for using lognormal or gamma distributions: The sensitivity is very weak, the vertical integrated fluxes change less than 1%, whereas the maximum heating rates change locally up to 15%.

[36] For testing the sensitivity due to different habits of ice crystals, we multiplied the derived effective radii by a constant factor $f = 0.5–1.5$ to estimate the change in habits which would translate into changes in the effective radius. This range is quite reasonable, as we can see from parameterizations for the effective ice crystal radius [e.g., *Sun and Shine*, 1995; *Gayet et al.*, 1996; *McFarlane et al.*, 1992]. Using this variation as shown in Figure 11 for a case with N = 1000L^{-1} and 100% of the maximal IWC: The outgoing longwave radiation, the reflected solar radiation and the net outgoing radiation at TOA changes in the ranges −15/+9%, +27/−13% and +7/−3%, respectively, and the peak heating rates change between 2.1 and 0.65 K d^{-1} by varying f from 0.5 to 1.5 (Figure 11).

3.3. Impact of Cirrus Formed Artificially at Saturation

[37] Although the existence of ice supersaturation in clear air and the formation of ice crystals at high ice supersaturations is known, almost all cloud parameterizations used in large-scale general circulation models form cirrus at ice saturation. When the model produces a supersaturation layer in one time step a cirrus is formed converting the excess gas phase water vapor above the saturation pressure into cloud ice. Thus these schemes do not allow ice supersaturation but immediately reduce the water vapor pressure to its saturation pressure.

[38] This simple but common saturation adjustment parameterization leads to differences in the produced cloud ice mixing ratios, the number concentrations and the cloud cover in large-scale models than if ice supersaturations are allowed to be maintained [*Lohmann and Kärcher*, 2002]. Even if cirrus would form in nature, the moment of the formation is predicted earlier; because it forms at satura-

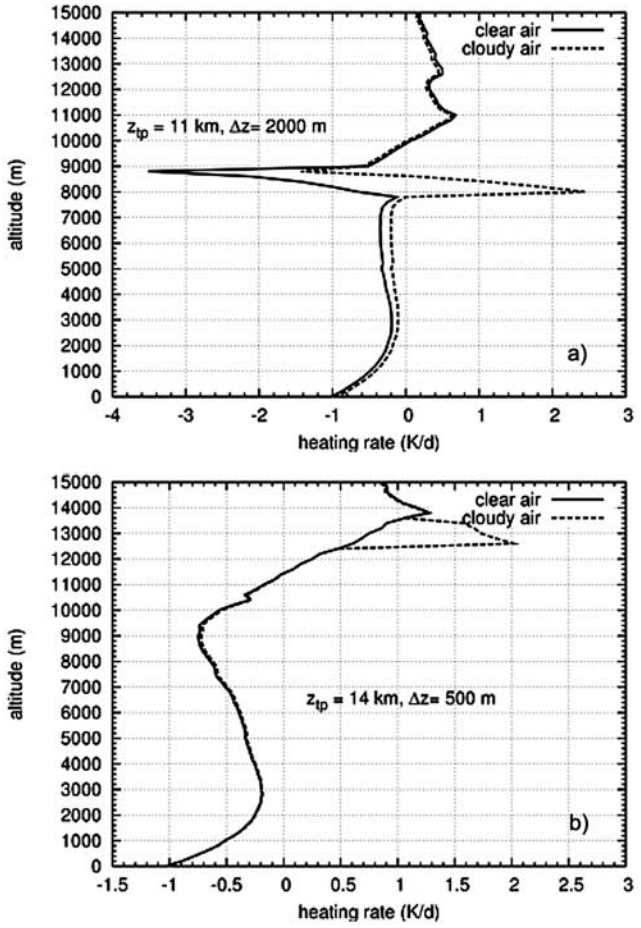

Figure 12. Net heating rate for ISSRs and cirrus formed at saturation by the model. (top) (Super-) saturated layer between 8 and 9 km, tropopause at 11 km. (bottom) (Super-) saturated layer between 12.5 and 13.5 km, tropopause at 14 km. Δz denotes the distance of the layer from the tropopause.

tion and not only after reaching the onset critical supersaturation for heterogeneous or homogeneous nucleation.

[39] Cloud free ice supersaturation can last for long times; in principle, once formed (i.e., RHi > 100%) it could last for hours to days, if there were no ice crystals inside the ISSR (by nucleation or sedimentation) and the relative humidity was not decreased by warming or mixing. Unfortunately, there is no information about the mean lifetime of ISSRs. There were only two case studies indicating different types of life cycles [*Spichtinger et al.*, 2005a, 2005b] embedded in different dynamical environments (synoptic dynamics: life time $\approx 24 \pm 3$ h, mesoscale dynamics: life time $\approx 6 \pm 3$ h).

[40] Nevertheless, ISSRs are frequently found in nature (up to 30% over the North Atlantic corridor [see *Gierens et al.*, 2000]) and also in global models, if supersaturation is allowed [*Lohmann and Kärcher*, 2002]. The frequency of occurrence in the GCM compares very well with measurements [*Gierens et al.*, 1999, 2000]; hence we get an idea how often ISSRs would occur in the global simulations. In fact, over the North Atlantic corridor, we found ice supersaturation in clear air in about 10–15% of the time.

[41] Here, we want to focus on the impact of cirrus formed in a saturation adjustment scheme during a synoptic updraft, as it can be observed for various synoptic conditions [e.g. *Spichtinger et al.*, 2005a] in the midlatitudes. For large-scale (or synoptic) updrafts, the vertical velocity is in the range $w <$ 10 cm s^{-1} as indicated by *Kärcher and Lohmann* [2002, Figure 7]. For an estimation of the impact of the cirrus formed by the adjustment scheme instead of having an ISSR we use a conceptual column model: We prescribe an idealized temperature profile according to *Clark and Farley* [1984] in the vertical range up to z = 30 km using a constant Brunt-Väisälä frequency of $N = 0.0094$ s^{-1} with a surface value of $T_{srf} = 293$ K and varying tropopause heights z_{TP} between 11 and 14 km. This conditions are very similar to the idealized temperature profile used in the sections above. This profile is typical for the midlatitudes.

[42] Additionally, we assume a RHi profile with a 1 km thick saturated layer 500–2000 m below the tropopause. Below the saturated layer we assume a constant value of $RHi = 60\%$ and above the layer we assume a constant value of $RHi = 20\%$ up to the tropopause. The specific humidity reaches values of ~6 ppm in the stratosphere.

[43] The supersaturated layer was cooled because of a constant vertical updraft of $w = 6.5$ cm s^{-1} (a moderate but common synoptic updraft) of the whole column for a whole GCM model time step. Here, we use a time step of dt = 24 min, which is the time step used at a spectral resolution of T42 of ECHAM GCM [*Roeckner et al.*, 2005]. The cooling rate is derived by $dT/dt = dT/dz \cdot dz/dt = -g/c_p \cdot w$.

[44] This causes a supersaturation of the layer that was initially saturated. The supersaturation reached depends strongly on the temperature within the layer, but in all different setups the values of RHi do not exceed RHi = 115%; the largest values were found for ISSRs at the highest altitudes, i.e., at the lowest temperatures.

[45] In order to determine the impact of cirrus formed at saturation on the radiation budget we assume that the ice supersaturation formed during one GCM model time step is completely transferred into the ice phase; that is, the newly formed cloud ice can be described as $q_c = q_v - q_s(T)$, where q_c, q_v and q_s denote mixing ratios of cloud ice, gas phase water vapor and saturation water vapor, respectively. For the radiation transfer model we also have to specify the effective radius. For this purpose we use the parameterization from the ECHAM model; that is, the effective radius is diagnosed from the ice water content via [*Lohmann et al.*, 1999]

$$r_{eff} = a \cdot \left(\frac{\mathrm{IWC}}{\mathrm{IWC}_0}\right)^b ; a = 83.8\mu\mathrm{m},\ b = 0.216,\ \mathrm{IWC}_0 = 1\mathrm{gm}^{-3} \tag{7}$$

We have used this formulation for consistency with the GCM model; in order to estimate the radiative impact of the artificially formed cirrus cloud in GCMs.

[46] The cloud free ISSR is then compared with thin cirrus as described in section 3.2. The supersaturations derived during a GCM model time step are much smaller (RHi < 115%) than the supersaturations in section 3.1 (RHi = 130–160%). Also the ice water content derived from the adjustment scheme is about two times smaller than the values obtained from the formula (1) used in section 3.2. Neverthe-

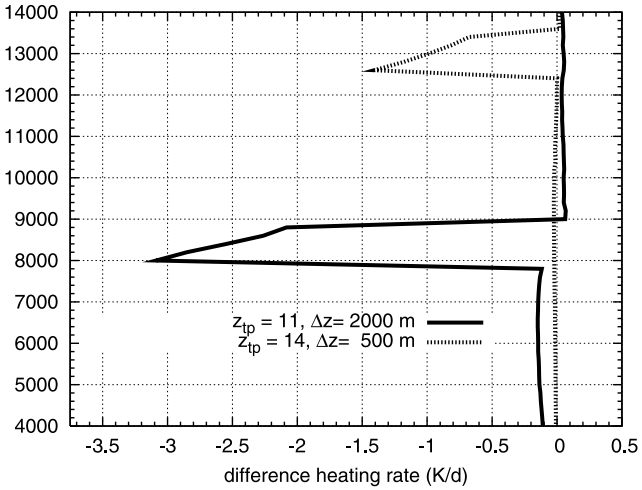

Figure 13. Differences in the net heating rates between the cloud free profile and the profile including artificially formed cirrus. Δz denotes the distance of the layer from the tropopause.

less, the formed cirrus is thick enough to have an impact on the radiation budget:

[47] In Figure 12 the net heating rates for the ice supersaturated layer in clear air and the artificially formed cirrus (with RHi = 100% inside the cloud) are shown for different cases, which roughly represent more or less the maximum and minimum impact (low altitude versus high altitude). The differences between clear (but supersaturated) and cloudy (but saturated) air are shown in Figure 13. The cirrus has a strong impact on the vertical net heating rate, the differences are in the range between 1.4 and 3.2 K d^{-1}. Also the impact on the integrated values is remarkable: The OLR changes between 2.9 W m^{-2} and 37.9 W m^{-2}, the net surface budget changes between 2.5 W m^{-2} and 40.9 W m^{-2} and the optical thickness of the incorrectly formed cirrus ranges between $\tau = 0.61$ and $\tau = 0.03$. The changes in all properties (integrated and local) show that artificially formed cirrus can strongly influence the radiative properties. Estimating the radiative impact in the full GCM is beyond the scope of this study but will be done in future.

[48] As mentioned before, the artificially formed cirrus have different properties, as was found by *Lohmann and Kärcher* [2002]: The ice water content and the ice crystal number concentration (calculated from the parameterization for the effective radius) were much higher and the cloud cover lower than for global simulations with a scheme including ISSRs.

[49] Currently, only few large-scale models treat the formation of cirrus in a physical way. This could lead to errors in the radiation properties. Therefore we recommend the use of a more physical parameterization of cirrus that allows supersaturation with respect to ice.

4. Summary and Conclusions

[50] In this study we have investigated the impact of ISSRs and thin cirrus on the radiation budget. For this purpose we used corrected radiosonde profiles for statistical investigations and constructed average supersaturation profiles with a supersaturated layer centered at the average altitude of 8200 m, with a vertical extension of 1200 m and a fixed but variable maximum relative humidity with respect to ice between 80 and 130%. This profiles was used in order to obtain the general features of the radiative properties of ice supersaturated regions and thin cirrus containing ice supersaturation. Additionally, we investigated possible errors in the radiation budget due to incorrectly parameterized cirrus in large-scale models.

[51] From our investigations we could answer some questions concerning the radiative impact of ISSRs and thin cirrus:

[52] 1. The impact of ice supersaturation on the surface is negligible.

[53] 2. There is a small effect on the outgoing longwave radiation due to ISSRs which might be interesting for remote sensing.

[54] 3. In the vertical profiles we found changes in the longwave heating rates up to 1 K d^{-1} for RHi = 130% compared to the saturated profiles. These changes in the heating rates could affect the local dynamics under certain conditions and could trigger the formation of thin cirrus due to radiative cooling at the top of the supersaturated layer.

[55] 4. The radiative impact of (even) thin cirrus is much stronger than for ISSRs and depends strongly on ice water content and ice crystal number concentration. In our calculations the optical depth can vary between 1.31 and 0.016, the values of OLR are between 189 W m^{-2} and 250 W m^{-2} and the reflected shortwave radiation reaches values between 130 W m^{-2} and 200 W m^{-2}. For small number concentrations $N < 320$ L^{-1} this causes a net warming in our scenarios whereas for larger crystal densities the shortwave cooling dominates. These results are weakly sensitive to changes in the shape of the size distribution. We found a stronger sensitivity for changes in the habit of the ice crystals.

[56] 5. Cirrus formed by a saturation adjustment scheme in large-scale model can produce large errors in the integrated fluxes and in the vertical profiles of the heating rates. Changes compared to the cloud free ISSR up to +8 K d^{-1} in the vertical profiles of net heating rates are possible, whereas changes in OLR and net surface budget up to 38 W m^{-2} or 41 W m^{-2}, respectively, are possible.

[57] There were some previous studies concerning the radiative impact of thin cirrus. Most of them are based on measurements [e.g., *Ackerman et al.*, 1988; *McFarquhar et al.*, 2000; *Hartmann et al.*, 2001] but there are also some model studies [*Gu and Liou*, 2000; *Liu et al.*, 2003]. Almost all studies using measurements focus on the tropics, hence it is quite hard to compare our results to these studies. However, the net heating rates derived for thin tropical cirrus are in the same order of magnitude as the heating rates derived for midlatitudes. The temperature profiles and the ice clouds simulated in the modeling studies by *Gu and Liou* [2000] and *Liu et al.* [2003] are close to our "midlatitude" scenario as are the quantitative values of the heating rates.

[58] A general estimate on the radiative impact of ISSRs and thin cirrus as, e.g., in the work by *Gettelman and Kinnison* [2006] could not derived, because we only have data from one location in the Northern Hemisphere midlatitudes. However, this study provides a first impression of the radiative impact of ISSRs and this cirrus and possible

errors in GCM due to non–physically based cirrus cloud parameterization.

[59] As we have shown, the radiative influence of ISSRs could lead to local changes in the vertical profiles of heating rates. For further investigations we will introduce a radiation transfer model into a cloud resolving cirrus cloud model to investigate the radiative impact on the vertical profiles and on the local dynamics.

Appendix A: Derivation of Effective Radius

[60] The effective radius defined by *Ebert and Curry* [1992] can be calculated using the integral expression but here we simplified this expression for obtaining a formula that depends only on the moments of the used size distribution.

[61] In general we assume columnar shaped crystals, i.e., small cylinders of length L and a hexagonal base with diameter D using again the definition of the effective radius by *Ebert and Curry* [1992] for randomly oriented small hexagonal columns:

$$r_{eff} = \frac{\int_0^\infty \left(\frac{A}{4\pi}\right)^{3/2} \cdot f(L)\, dL}{\int_0^\infty \frac{A}{4\pi} \cdot f(L)\, dL}$$

A denotes the whole surface area of the column. Using the mass-size relation equation (3), the geometry of a columnar ice crystal and the definition of the aspect ratio of a single ice crystal one can derive an expression for the aspect ratio r_a: = L/D depending on the ice crystal size:

$$r_a(L) = C(\rho_b) \cdot L^{\frac{3-\beta}{\beta}} \tag{A1}$$

where $\rho_b = 0.81$ g cm^{-3} denotes the bulk density of ice.

[62] Hence we can express the whole surface area of a hexagonal column A and the term $A^{\frac{3}{2}}$ using the length L and the aspect ratio r_a of the ice crystals:

$$A = 6\left(\frac{\sqrt{3}}{2} \cdot a^2 + a \cdot L\right) = 3\frac{L^2}{r_a}\left(1 + \frac{\sqrt{3}}{4r_a}\right) \tag{A2}$$

$$A^{\frac{3}{2}} \approx \sqrt{27}\left(\frac{L^2}{r_a}\right)^{\frac{3}{2}} \cdot \left(1 + \frac{\sqrt{27}}{8r_a} + \frac{9}{128r_a^2}\right) \tag{A3}$$

the latter expression is due to a Taylor expansion with second-order approximation. Using these terms, the effective radius can be written in terms of general moments $\mu_k[L]$: = $\int f(L)L^k dL$ of the ice crystal mass distribution:

$$r_{eff} \approx \frac{1}{2\sqrt{\pi}} \frac{C_{11} \cdot \mu_{\frac{3(\beta+1)}{4}}[L] + C_{12} \cdot \mu_{\frac{5\beta-3}{4}}[L] + C_{13} \cdot \mu_{\frac{7\beta-9}{4}}[L]}{C_{21} \cdot \mu_{\frac{\beta+1}{2}}[L] + C_{22} \cdot \mu_{\beta-1}[L]} \tag{A4}$$

where $C_i = C_i(\rho_b, \alpha, \beta)$ denote some constants depending only on the bulk ice density and the coefficients of the mass-size-relation equation (3). Now, for a distribution with an analytical expression for the moments, this general formula can be used. Note that for variable α, β (e.g., piecewise constant) equation (11) can be expressed using truncated moments of the lognormal distribution [*Jawitz*, 2004].

[63] **Acknowledgments.** We thank Andreas Mühlbauer for assistance concerning statistics. We thank Marian DeReus, Felix Seidel and Klaus Itten for fruitful discussions. We thank Qiang Fu for providing us with his radiation transfer model. We also thank three anonymous reviewer for helpful suggestions. This article contributes to the special issue of the "Second international conference on global warming and the next ice age" at Santa Fe, 2006.

References

Ackerman, T., K.-N. Liou, F. Valero, and L. Pfister (1988), Heating rates in tropical anvils, *J. Atmos. Sci.*, *45*, 1606–1623.

Antikainen, V., and H. Jauhiainen (1995), Vaisala's new RS90 family of radiosondes, *Vaisala News*, *136*, 9–12.

Chen, T., W. B. Rossow, and Y. Zhang (2000), Radiative effects of cloud-type variations, *J. Clim.*, *13*, 264–286.

Clark, T., and R. Farley (1984), Severe downslope wind- storm calculations in two and three spatial dimensions using anelastic interactive grid nesting: A possible mechanism for gustiness, *J. Atmos. Sci.*, *41*, 329–350.

Comstock, J. M., T. P. Ackerman, and D. D. Turner (2004), Evidence of high ice supersaturation in cirrus clouds using ARM Raman lidar measurements, *Geophys. Res. Lett.*, *31*, L11106, doi:10.1029/2004GL019705.

DeMott, P., D. Cziczo, A. Prenni, D. Murphy, S. Kreidenweis, D. Thomson, R. Borys, and D. Rogers (2003), Measurements of the concentration and composition of nuclei for cirrus formation, *Proc. Natl. Acad. Sci. U. S. A.*, *100*(25), 14,655–14,660.

Dobbie, J. S., J. N. Li, and P. Chylek (1999), Two- and four-stream optical properties for water clouds and solar wavelengths, *J. Geophys. Res.*, *104*, 2067–2079.

Dowling, D. R., and F. L. Radke (1990), A summary of the physical properties of cirrus clouds, *J. Appl. Meteorol.*, *29*, 970–978.

Ebert, E. E., and J. A. Curry (1992), A parametrization of ice cloud optical properties for climate models, *J. Geophys. Res.*, *97*, 3831–3836.

Forster, de F. P., and J. M. Gregory (2006), The climate sensitivity and its components diagnosed from Earth radiation budget data, *J. Clim.*, *19*, 39–52.

Fu, Q. A. (1996), An accurate parameterization of the solar radiative properties of cirrus clouds for climate models, *J. Clim.*, *9*, 2058–2082.

Gayet, J.-F., G. Febvre, G. Brogniez, H. Chepfer, W. Renger, and P. Wendling (1996), Microphysical and optical properties of cirrus and contrails: Cloud field study on 13 October 1989, *J. Atmos. Sci.*, *53*, 126–138.

Gettelman, A., and D. E. Kinnison (2006), The global impact of supersaturation in a coupled chemistry-climate model, *Atmos. Chem. Phys. Disc.*, *6*, 12,433–12,468.

Gettelman, A., V. P. Walden, L. M. Miloshevich, W. L. Roth, and B. Halter (2006), Relative humidity over Antarctica from radiosondes, satellites, and a general circulation model, *J. Geophys. Res.*, *111*, D09S13, doi:10.1029/2005JD006636.

Gierens, K., and P. Spichtinger (2000), On the size distribution of ice supersaturation regions in the upper troposphere and lower stratosphere, *Ann. Geophys.*, *18*, 499–504.

Gierens, K., U. Schumann, M. Helten, H. Smit, and A. Marenco (1999), A distribution law for relative humidity in the upper troposphere and lower stratosphere derived from three years of MOZAIC measurements, *Ann. Geophys.*, *17*, 1218–1226.

Gierens, K., U. Schumann, M. Helten, H. Smit, and P.-H. Wang (2000), Ice-supersaturated regions and subvisible cirrus in the northern midlatitude upper troposphere, *J. Geophys. Res.*, *105*, 22,743–22,753.

Glückauf, E. (1945), Notes on upper air hygrometry—II: On the humidity in the stratosphere, *Q. J. R. Meteorol. Soc.*, *71*, 110–112.

Gu, Y., and K. Liou (2000), Interactions of radiation, microphysics, and turbulence in the evolution of cirrus clouds, *J. Atmos. Sci.*, *57*, 2463–2479.

Hartmann, D., J. Holton, and Q. Fu (2001), The heat balance of the tropical tropopause, cirrus and stratospheric dehydration, *Geophys. Res. Lett.*, *28*, 1969–1972.

Heymsfield, A. J., and J. Iaquinta (2000), Cirrus crystal terminal velocities, *J. Atmos. Sci.*, *57*, 916–938.

Jawitz, J. W. (2004), Moments of truncated continuous univariate distributions, *Adv. Water Resour.*, *27*(3), 269–281.

Jensen, E. J., et al. (1998), Ice nucleation processes in upper tropospheric wave-clouds during SUCCESS, *Geophys. Res. Lett.*, *25*, 1363–1366.

Kärcher, B., and U. Lohmann (2002), A parameterization of cirrus cloud formation: Homogeneous freezing of supercooled aerosols, *J. Geophys. Res.*, *107*(D2), 4010, doi:10.1029/2001JD000470.

Koop, T., B. Luo, A. Tsias, and T. Peter (2000), Water activity as the determinant for homogeneous ice nucleation in aqueous solutions, *Nature*, *406*, 611–614.

Leiterer, U., H. Dier, D. Nagel, T. Naebert, D. Althausen, K. Franke, A. Kats, and F. Wagner (2005), Correction method for RS80—A humicap humidity profiles and their validation by lidar backscattering profiles in tropical cirrus clouds, *J. Atmos. Oceanic Technol.*, *22*(1), 18–29.

Liu, H.-C., P. Wang, and R. Schlesinger (2003), A numerical study of cirrus clouds. Part II: Effects of ambient temperature, stability, radiation, ice microphysics, and microdynamics on cirrus evolution, *J. Atmos. Sci.*, *60*, 1097–1119.

Liu, X., J. E. Penner, S. J. Ghan, and M. Wang (2007), Inclusion of ice microphysics in the NCAR Community Atmospheric Model Version 3 (CAM3), *J. Clim.*, *20*, 4526–4547.

Lohmann, U., and B. Kärcher (2002), First interactive simulations of cirrus clouds formed by homogeneous freezing in the ECHAM general circulation model, *J. Geophys. Res.*, *107*(D10), 4105, doi:10.1029/2001JD000767.

Lohmann, U., N. McFarlane, L. Levkov, K. Abdella, and F. Albers (1999), Comparing different cloud schemes of a single column model by using mesoscale forcing and nudging technique, *J. Clim.*, *12*, 438–461.

Mace, G., S. Benson, and E. Vernon (2006), Cirrus clouds and the large-scale atmospheric state: Relationships revealed by six years of ground-based data, *J. Clim.*, *19*, 3257–3278.

McFarlane, N. A., G. J. Boer, J. P. Blanchet, and M. Lazare (1992), The Canadian Climate Centre Second-Generation General Circulation Model and its equilibrium climate, *J. Clim.*, *5*, 1013–1044.

McFarquhar, G. M., A. J. Heymsfield, J. Spinhirne, and B. Hart (2000), Thin and subvisible tropopause tropical cirrus: Observations and radiative impact, *J. Atmos. Sci.*, *57*, 1841–1853.

Möhler, O., P. R. Field, P. Connolly, S. Benz, H. Saathoff, M. Wagner, R. Cotton, M. Kraemer, A. Mangold, and A. J. Heymsfield (2006), Efficiency of the deposition mode ice nucleation on mineral dust particles, *Atmos. Chem. Phys.*, *6*, 3007–3021.

Ovarlez, J., P. van Velthoven, G. Sachse, S. Vay, H. Schlager, and H. Ovarlez (2000), Comparison of water vapor measurements from POLINAT 2 with ECMWF analyses in high humidity conditions, *J. Geophys. Res.*, *105*, 3737–3744.

Ovarlez, J., J.-F. Gayet, K. Gierens, J. Ström, H. Ovarlez, F. Auriol, R. Busen, and U. Schumann (2002), Water vapour measurements inside cirrus clouds in Northern and Southern hemispheres during INCA, *Geophys. Res. Lett.*, *29*(16), 1813, doi:10.1029/2001GL014440.

Peter, T., C. Marcolli, P. Spichtinger, T. Corti, M. B. Baker, and T. Koop (2006), When dry air is too humid, *Science*, *314*(5804), 1399–1400.

Pruppacher, H. (1995), A new look at homogeneous ice nucleation in supercooled water drops, *J. Atmos. Sci.*, *52*, 1924–1933.

Quante, M. (2004), The role of clouds in the climate system, *J. Phys. IV*, *121*, 61–86.

Roeckner, E., et al. (2005), The atmospheric general circulation model ECHAM 5. Part I: Model description, *MPI Rep. 439*, Max Planck Inst. for Meteorol., Hamburg, Germany.

Schumann, U. (2002), Contrail cirrus, in *Cirrus*, edited by D. K. Lynch et al., pp. 231–255, Oxford Univ. Press, Oxford, U. K.

Slingo, A. (1989), A GCM parameterization for the shortwave radiative properties of water clouds, *J. Atmos. Sci.*, *46*, 1419–1427.

Soden, B. J., D. L. Jackson, V. Ramaswamy, M. D. Schwarzkopf, and X. L. Huang (2005), The radiative signature of upper tropospheric moistening, *Science*, *310*(5749), 841–844.

Spichtinger, P., K. Gierens, U. Leiterer, and H. Dier (2003a), Ice supersaturation in the tropopause region over Lindenberg, Germany, *Meteorol. Z.*, *12*, 143–156.

Spichtinger, P., K. Gierens, and W. Read (2003b), The global distribution of ice supersaturated regions as seen by the microwave limb sounder, *Q. J. R. Meteorol. Soc.*, *129*, 3391–3410.

Spichtinger, P., K. Gierens, H. G. J. Smit, J. Ovarlez, and J.-F. Gayet (2004), On the distribution of relative humidity in cirrus clouds, *Atmos. Chem. Phys.*, *4*, 639–647.

Spichtinger, P., K. Gierens, and H. Wernli (2005a), A case study on the formation and evolution of ice supersaturation in the vicinity of a warm conveyor belt's outflow region, *Atmos. Chem. Phys.*, *5*, 973–987.

Spichtinger, P., K. Gierens, and A. Dörnbrack (2005b), Formation of ice supersaturation by mesoscale gravity waves, *Atmos. Chem. Phys.*, *5*, 1243–1255.

Stephens, G. L., and P. J. Webster (1981), Clouds and climate—Sensitivity of simple systems, *J. Atmos. Sci.*, *38*, 235–247.

Sun, Z., and K. Shine (1995), Studies of the radiative properties of ice and mixed-phase clouds, *Q. J. R. Meteorol. Soc.*, *515*, 111–137.

Tompkins, A., K. Gierens, and G. Radel (2007), Ice supersaturation in the ECMWF integrated forecast system, *Q. J. R. Meteorol. Soc.*, *133*, 53–63.

Vay, S. A., B. E. Anderson, E. J. Jensen, G. W. Sachse, J. Ovarlez, G. L. Gregory, S. R. Nolf, J. R. Podolske, T. A. Slate, and C. E. Sorenson (2000), Tropospheric water vapor measurements over the North Atlantic during the Subsonic Assessment Ozone and Nitrogen Oxide Experiment (SONEX), *J. Geophys. Res.*, *105*, 3745–3756.

Verlinde, J., et al. (2007), The Mixed-Phase Arctic Cloud Experiment, *Bull. Am. Meteorol. Soc.*, *82*, 205–221.

Wall, E. (1942), Material zur Frage der Eiskeimbildung in der Atmosphäre, *Meteorol. Z.*, *59*(4), 109–120.

Wyser, K. (1998), The effective radius in ice clouds, *J. Clim.*, *12*, 1793–1802.

Zhang, J., U. Lohmann, and P. Stier (2005), A microphysical parameterization for convective clouds in the ECHAM5 climate model: Single-column model results evaluated at the Oklahoma Atmospheric Radiation Measurement Program site, *J. Geophys. Res.*, *110*, D15S07, doi:10.1029/2004JD005128.

F. Fusina, U. Lohmann, and P. Spichtinger, Institute for Atmospheric and Climate Science, ETH Zurich, CH-8092 Zurich, Switzerland. (fabian.fusina@env.ethz.ch; ulrike.lohmann@env.ethz.ch; peter.spichtinger@env.ethz.ch)